



Full length article

Nanocalorimetry and *ab initio* study of ternary elements in CuZr-based shape memory alloy

Yucong Miao^a, Ruben Villarreal^b, Anjana Talapatra^b, Raymundo Arróyave^b,
Joost J. Vlassak^{a,*}

^a John A. Paulson School of Engineering and Applied Sciences, Harvard University, Cambridge, MA 02138, United States

^b Department of Materials Science and Engineering, Texas A&M University, College Station, TX 77843, United States

ARTICLE INFO

Article history:

Received 1 August 2019

Revised 9 October 2019

Accepted 13 October 2019

Available online 23 October 2019

Keywords:

Shape memory alloy

Nanocalorimetry

Ab initio simulation

Martensitic transformation

Twin boundary

ABSTRACT

We present a computational-experimental study on the ternary alloying effect of CuZr-based shape memory alloy. The transformation behavior, including crystallization, martensite-austenite transformation temperature and hysteresis of Cu-Zr-X (X = Ni, Co, Hf) thin-film samples were investigated by nanocalorimetry. We used *ab initio* simulations to determine the B2-Cm transformation pathway, evaluate the lattice parameters, the relative phase stability, and the twin boundary energy as a function of composition. Experimental results show that alloying with Ni or Co reduces the hysteresis of the martensitic transformation, while Hf increases it. These observations are in agreement with the trend of the middle eigenvalue of the martensitic transformation matrix. The energy difference between the pure phases obtained from simulations suggests that both Co and Ni stabilize martensite against austenite. However, experiments show that Co decreases transformation temperature, while Ni increases it. We attribute this observation to the larger twin boundary energy and strain energy in the Co-containing alloy. Our results indicate that *ab initio* simulations are a helpful tool in the development of new shape memory alloys, provided the energy terms associated with the fine twin structure of the martensite are taken into account.

© 2019 Acta Materialia Inc. Published by Elsevier Ltd. All rights reserved.

1. Introduction

Shape memory alloys (SMAs) undergo large recoverable shape changes as a result of a thermoelastic martensitic transformation that may be induced by changes in temperature, stress, or even magnetic field in the case of ferromagnetic alloys. The martensitic transformation is characterized by a reduction in lattice symmetry as the material transforms from the high-temperature austenitic phase to the low-temperature martensitic phase, and has a strong deviatoric component. Despite intensive research efforts in recent years, the subset of SMAs that transform above 100 °C, known as high-temperature SMAs (HTSMAs), remains relatively unexplored [1]. Recently, HTSMAs have attracted significant interest due to their potential use in high-temperature solid-state actuators that are more efficient, light-weight, and robust than conventional actuators [1–4]. HTSMAs will enable a wide range of critical technologies for both civilian and defense applications, including adaptable wings, low-volume, high-energy-density actuation, and energy harvesting through exploitation of the elasto-caloric effect

[2,5,6]. In addition to high transformation temperatures, potential HTSMAs must also exhibit acceptable recoverable transformation strain levels, long-term stability, low thermal hysteresis, good creep resistance, low susceptibility to plastic deformation, and adequate resistance to environmental conditions [1]. It is clear from this list of requirements that developing new HTSMAs is not trivial. The chemical composition space that needs to be searched to satisfy these requirements is too large to be explored solely by experimental means. A number of material descriptors including valence electron concentration, average Pauling electronegativity, and atomic size have been shown to correlate with transformation temperature and can be used to guide experiments [7], but these descriptors are not necessarily predictive for more complex alloys [8]. Evidently, these descriptors do not fully capture the physics of the transformations.

In this work, we used a combination of nanocalorimetry and *ab initio* simulations to investigate the effects of ternary alloying elements on the transformation behavior of CuZr-based shape memory alloys. Nanocalorimetry is used to measure the transformation behavior in thin-film samples of Cu-Zr-X (X = Ni, Co, Hf). Samples are fabricated using magnetron sputtering, which allows synthesis of samples over a wide range of compositions. Thin-film samples typically have a much finer microstructure than bulk

* Corresponding author.

E-mail address: vlassak@seas.harvard.edu (J.J. Vlassak).

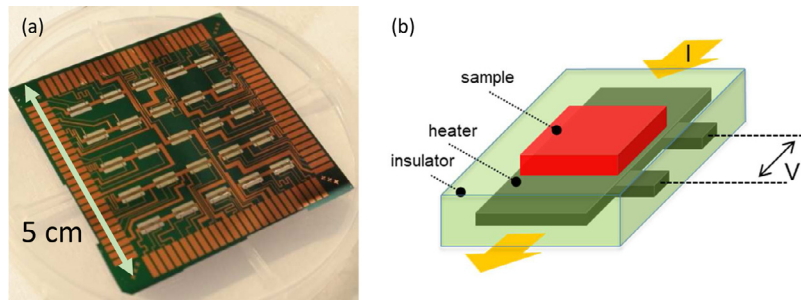


Fig. 1. (a) Array of 25 nanocalorimetry sensors and (b) schematic representation of an individual sensor.

specimens. While the distinctive microstructure of thin films has an impact on the transformation behavior of thin-film samples, the trends with changes in composition are similar to those observed in bulk samples [9,10]. The *ab initio* simulations provide insight into how the alloying elements change the energies of the participating phases. Simulations at 0 K show that Ni and Co lower the energy of the martensitic phase compared to the austenitic phase, while Hf leaves the energy nearly unchanged, suggesting that Ni and Co should increase the transformation temperatures (A_p) and that adding Hf should have little effect. These findings are confirmed by finite-temperature simulations. Experimental measurements, however, show that Co lowers A_p , while both Ni and Hf increase A_p . We suggest that this discrepancy is caused by the fact that the addition of Co increases the twin boundary energy and the strain energy associated with the austenite-martensite mismatch. We show that these energy terms can be calculated from *ab initio* simulations and incorporated into a more comprehensive model of the austenite-martensite transformation.

2. Methods

2.1. Nanocalorimetry

Nanocalorimetry measurements were performed on thin-film samples of Cu-Zr-X using custom-made micromachined calorimetry sensors described in detail elsewhere [11,12]. Fig. 1a shows an array of 5×5 sensors, each one of which is independently controlled. As shown schematically in Fig. 1b, each sensor consists of a thin W layer that is patterned to serve both as heating element and resistance thermometer in a four-point measurement scheme. This heating element/thermometer is encapsulated in a thin SiN_x membrane that supports the heating element and insulates it from its surroundings. The sample of interest is deposited in the area between the voltage leads as indicated in Fig. 1b. In a typical calorimetry scan, an electric current is supplied through the heating element, which causes Joule heating of the sample and addendum. The measured current and voltage are then used to determine the power to the sensor and the resistance of the heating element, which is calibrated to temperature. The temperature coefficient of resistance λ is determined by measuring the melting point of Ag on select sensors in the sensor array. Because of the linear behavior of the W heating element, this approach offers the same accuracy as a calibration inside a vacuum furnace, but is much faster. Within the same sensor array, the variation of λ is estimated to be less than 1%.

To perform the measurements, the sensor array is placed in a probe card that is located inside a vacuum chamber with a base pressure of approximately 10^{-4} Pa. The data are acquired using a custom-built system described in detail by Zheng et al. [12]. This data acquisition system uses a differential setup where the same current flows through a sensor with a sample and a reference sen-

sor connected in series. The system then measures the current I through both sensors, the voltage drop V_S across the sample sensor, the voltage drop V_R across the reference sensor, and the differential voltage $V_D = V_S - V_R$ using 24-bit A/D converters. The differential setup rejects the common noise between the two sensors and significantly improves the sensitivity of the measurement. Optimally, the 6-sigma noise level can be as low as 1.7 nJ/K at 400 K [12]. All measurements in this study are performed at heating rates between 3000 and 4000 K/s.

In the analysis, the temperature is determined from the temperature coefficient of resistance of the sensor heating element using,

$$R = R_0(1 + \lambda(T - T_0)), \quad (1)$$

where λ is the temperature coefficient of resistance, T is the temperature of the sensor, T_0 is the ambient temperature, R the resistance at T , and R_0 the resistance at T_0 . The energy balance for a single calorimetric sensor dictates that

$$P(T) = C_p\beta + H_R(T) + L(T) \quad (2)$$

during a measurement. In this expression, P denotes the power supplied to the sensor, C_p is heat capacity of the sample and sensor addendum, β is the heating rate, H_R is the heat flow associated with any reaction or phase transformation in the sample (taken positive for an endothermic reaction), and L represents any heat loss due to conduction and radiation. Eq. (2) can be used to obtain information on the heat capacity and enthalpy of transformation of a sample. A detailed data reduction procedure can be found in our previous work [12].

2.2. Sample preparation

Individual thin-film samples were synthesized directly on top of the calorimetry sensors by sputter deposition through a shadow mask. Prior to sample synthesis, a 20 nm layer of HfO₂ was grown on the sensors using atomic layer deposition (Cambridge NanoTech ALD System) to prevent reaction between the samples and the silicon nitride of the sensor. After HfO₂ deposition, the sensors were conditioned at 1300 K for a period of 10 s to ensure sensor stability. Cu-Zr-X samples with a thickness of approximately 400 nm were then deposited on top of the HfO₂-coated sensors by magnetron sputtering from elemental targets inside a vacuum chamber (ATC-1800, AJA Inc.) with a base pressure better than 10^{-4} Pa. A micromachined shadow mask was used to limit the deposition to the area of the sensor between the voltage probes. The depositions were performed at a pressure of 5 mTorr using argon that was filtered to 99.999% purity as a working gas. All deposition targets (Zr, Cu, Ni, Co, and Hf) were obtained from Kurt J. Lesker Co. with the highest purity available. The compositions of the samples were targeted to be Cu_{50-x}Zr₅₀Ni_x, Cu_{50-x}Zr₅₀Co_x, and Cu₅₀Zr_{50-x}Hf_x, and were measured using X-ray photoelectron

spectroscopy (XPS, Thermo Scientific K-Alpha Plus XPS System). The surfaces of the samples were sputtered with Ar inside the XPS chamber to expose pristine material for analysis.

2.3. *Ab initio* simulations

Ab initio simulations were performed using the Vienna *ab initio* Simulation Package (VASP) [13]. The exchange-correlation function of the pseudopotential was treated using the generalized gradient approximation (GGA) [14], and the core-valence interaction was treated using the projector augmented wave (PAW) method [15]. The electronic configurations of the appropriate elements were realized using the projector augmented-wave (PAW) pseudo-potentials formalism [16]. Full relaxations were realized by using the Methfessel-Paxton smearing method of order one [17] and self-consistent static calculations were carried out with the tetrahedron smearing method with Blöchl corrections [18]. A cutoff energy of 364 eV was used for all the calculations and spin polarizations were accounted for as well. The Brillouin zone integrations were performed with a mesh containing 3000 *k*-points per atom. Convergence of the electronic structure was assumed, when energy changes between two consecutive steps fell below 10^{-6} eV and ionic forces were at most 10^{-4} eV Å⁻¹ in absolute value.

First, we mapped the energy landscape of the CuZr austenite-martensite transformation. In accord with our TEM characterization (See Section 3.3) and previous observations [19,20], the space group of austenite was set to Pm3m (also known as B2), while that of martensite was set to Cm. The energy landscape for the transformations were modeled using a four-dimensional parametric model [21]. The Pm3m-Cm transformation, using a parent body-centered tetragonal (bct) lattice, consists of four independent motions: (i) a shuffle along $[110]_{B2}$, (ii) a shuffle along $[001]_{B2}$, (iii) an orthorhombic distortion (change in volume) and (iv) a monoclinic distortion. The parametrization was based on a linear interpolation scheme where supercells were chosen such that the linear difference of the internal coordinates was minimized. This model assumes that the displacive transformation can be characterized by a distinct separation between short range atomic shuffles and the lattice degrees of freedom, which include lattice strain, angular shear, and volume change. The energy landscape was constituted from 60 calculated points sampled from a $9 \times 9 \times 9 \times 9$ (four degrees of freedom) parameter space using the Latin hypercube sampling method [22]. Although this is considerably sparse, the energy landscapes show sufficient qualitative differences in the energy barriers found along the minimum energy paths (MEPs) when comparing different alloy compositions. A 4D MEP for CuZr was extracted from the landscape using a modified implementation of Dijkstra's algorithm [23]. The B2 and Cm structures were set as the source (target) nodes. The MEP was further refined by the use of the solid state nudged elastic band method (SSNEB) [24] and served as a good first approximation to the transformation pathway. The symmetries along the converged transformation pathway were found to be group-subgroup related with a transformation index of 96 as confirmed by the SubGroupGraph tool implemented in the Bilbao crystallographic server [25].

Next, we determined the lattice parameters and energies of Cu-Zr-X (X=Co, Ni, Hf). Depending on the alloy, supercells of sizes varying from 16 to 64 atoms were used. The input structures were the CuZr B2 and Cm phases with Co/Ni/Hf atom replacements of up to 18.75%. In the simulations, Co and Ni replaced Cu, while Hf replaced Zr. The resulting composition covers the range studied by nanocalorimetry. To best model the disorder caused by the ternary elements, two methods were used and compared against each other: 64-atom special quasi-random structures [26] and human decisions based on site symmetry and distance to neighbors.

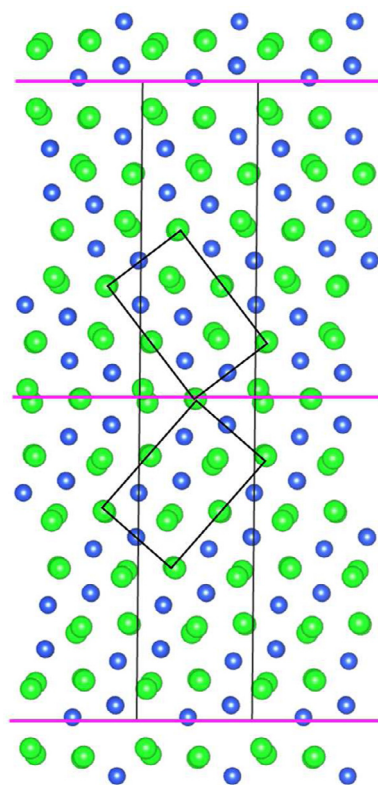


Fig. 2. CuZr supercell containing (021) twin boundaries. The volume between the two vertical black lines represents one supercell, while the mirrored unit cells represent the Cm structure. Due to periodic boundary condition, there is one twin plane in the middle and another twin plane at top/bottom.

Calculations of the finite-temperature energies for the Cu-Zr-X alloys were carried out considering the contributions of vibrational and electronic degrees of freedom to the total free energy of the system. The vibrational contributions to the free energy—derived from the phonon density of states—were calculated using the harmonic approximation, which assumes small atomic oscillations about the equilibrium value. The supercell method [27] as implemented in the *fitc* module of the ATAT package [28] was used to determine the phonon structure of the alloys under study. In this method, the positions of the atoms are slightly perturbed away from their equilibrium position and the reaction forces are calculated. A set of linear constraints are obtained by equating the calculated forces to the forces predicted from the harmonic model. From these, the unknown force constants are determined. The force constant tensor is then used to determine the dynamical matrix whose diagonalization yields the eigenvalues (frequencies) and eigenvectors (displacements) of the normal modes of oscillation (phonons) [29]. To account for the softening of the phonon modes due to thermal expansion, the quasi-harmonic approximation was used [29]. In this approximation, the optimized structures are subjected to expansion and contraction and harmonic calculations are performed on each of the corresponding volumes. Specifically, three volumes were considered, which were equally spaced from 2% to 4% of the equilibrium volume. For a detailed discussion of the method, one may refer to [30].

The twin boundary energies of Cu-Zr-X were calculated using an 88 atom supercell that consists of (021) twin planes. Fig. 2 shows the structure of the supercell under periodic boundary condition. The structure is built using the same parameters as the untwinned Cu-Zr-X supercell. The top/bottom and middle planes are two twin planes with a spacing of 1.35 nm. The atomic positions and volume are relaxed, while the shape is kept unchanged to

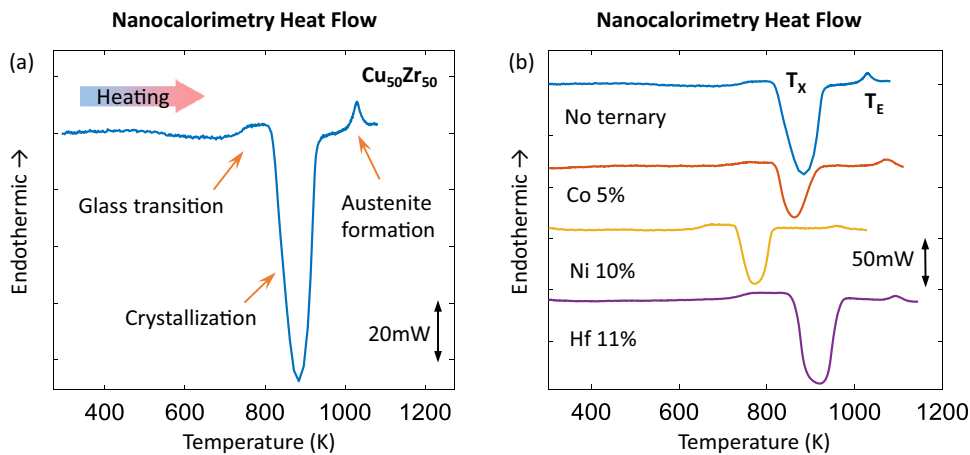


Fig. 3. (a) First calorimetry scan on an as-deposited $\text{Cu}_{50}\text{Zr}_{50}$ sample and (b) first scans on as-deposited samples of several different CuZr-based alloys.

retain the twin structure. The twin boundary energy is found by subtracting the energy of the untwinned structure (linear fit of all data points) from the twinned structure.

3. Results

3.1. Cu-Zr-X phase evolution

Fig. 3a shows a typical first calorimetry scan on an as-deposited $\text{Cu}_{50}\text{Zr}_{50}$ sample; Fig. 3b depicts similar scans for as-deposited samples of several ternary Cu-Zr-X alloys. It is evident from the figures that all Cu-Zr-X samples go through a similar series of reactions in the first scan – all scans have a strong exothermic peak followed by a smaller endothermic peak at more elevated temperature. Previous studies on CuZr-based alloys have shown that samples sputter-deposited under similar conditions are amorphous and that the large peak in the calorimetry trace corresponds to the crystallization of the samples. Immediately prior to crystallization, there is a small change in heat capacity of the samples, which is caused by the glass transition [31,32]. In the case of $\text{Cu}_{50}\text{Zr}_{50}$, the crystallization products are CuZr_2 (space group I4/mmm) and $\text{Cu}_{10}\text{Zr}_7$ (space group Cmca). At higher temperature, these phases react endothermically to form the ordered CuZr austenitic phase (space group Pm3m, also known as B2) in a eutectoid process [12]. Given the relatively small alloy additions and the fact that CuHf_2 , $\text{Cu}_{10}\text{Hf}_7$, NiZr_2 , $\text{Ni}_{10}\text{Zr}_7$, and CoZr_2 are all stable phases with the same structures as CuZr_2 and $\text{Cu}_{10}\text{Zr}_7$ (except for $\text{Co}_{10}\text{Zr}_7$) [33–35], it is likely that the small endothermic peak after the crystallization peak in Fig. 3b represents a eutectoid reaction similar to that found in the CuZr system.

None of the samples shows a martensitic transformation if they are cooled immediately after the formation of the austenitic phase. In the case of $\text{Cu}_{50-x}\text{Zr}_{50}\text{Ni}_x$ samples, a heat treatment of 20 s at 1100 K is needed before the martensitic transformation is observed. In the case of $\text{Cu}_{50-x}\text{Zr}_{50}\text{Co}_x$ and $\text{Cu}_{50}\text{Zr}_{50-x}\text{Hf}_x$, the samples are partially melted and re-solidified to show the martensitic transformation. We suggest that the B2 phase formed in the eutectoid reaction has too many defects to allow transformation to martensite on cooling. Possible causes are: (1) the austenitic phase is not fully stoichiometric as the B2 phase forms by reaction of Zr- and Cu-rich phases and the composition may not be completely uniform; (2) insufficient ordering of the B2 phase. Either possibility indicates that the solid-state reaction needs a sufficiently long time to complete without giving a measurable calorimetric signal. This observation is not entirely surprising given that binary CuZr is a very good glass former and is expected to have sluggish kinetics [32,36].

The crystallization temperature of Cu-Zr-X gives an indication of the glass forming ability of the Ni, Co, and Hf-containing ternaries. Of the three alloys, Cu-Zr-Ni has the lowest crystallization temperature, i.e., the fastest kinetics, and presumably the poorest glass forming ability. Therefore, a very brief heat treatment of Cu-Zr-Ni at 1100 K is sufficient to create an austenite that transforms to martensite at low temperature. Presumably, a longer treatment at 1100 K would result in the formation of martensite for the Co- and Hf-containing ternaries also, but such a treatment would lead to excessive oxidation of the samples. By contrast, previous studies on bulk samples of ternary Cu-Zr-X alloys used arc melting followed by annealing at 1100 K for 30 min or longer [37,38].

3.2. Transformation temperatures and hysteresis

Fig. 4a shows calorimetry traces for several alloys with the martensite to austenite transformation on heating; Fig. 4b shows a graph of the transformation temperature as a function of composition. It is evident from the figure that replacing Cu with Ni or Zr with Hf increases the transformation temperature, although the effect of Hf is weaker than that of Ni. Replacing Cu with Co, on the other hand, slightly lowers the transformation temperature. The sample with 8% Co did not show a transformation even after being cooled to 150 K. Similar trends have been reported in previous studies on bulk Cu-Zr-X samples [8,37,39–41], although the changes in transformation temperature brought about by ternary element addition tend to be larger in bulk samples than in thin films. This is likely due to the smaller grain size observed in thin films, which is well-known to depress transformation temperatures in shape memory alloys [9,10].

Fig. 5 shows the hysteresis as determined by the temperature difference between the transformations on heating and cooling. The addition of Ni and Co decreases the hysteresis, while Hf increases it. The hysteresis observed for bulk CuZr alloys in previous studies ranges from 115 K to 250 K and depends on both heat treatment and the number of thermal cycles performed [37–39,42]. The hysteresis measured in this study is at the upper limit of this range, possibly due to small grain size of the thin-film samples [43].

3.3. Microstructure

Fig. 6 shows TEM images of cross-sectional samples with compositions $\text{Zr}_{50}\text{Cu}_{34}\text{Ni}_{16}$ and $\text{Cu}_{50}\text{Zr}_{39}\text{Hf}_{11}$. Both images show clearly-defined martensitic plates, with widths ranging from 30 to 60 nm. The Hf-containing sample has slightly wider martensitic

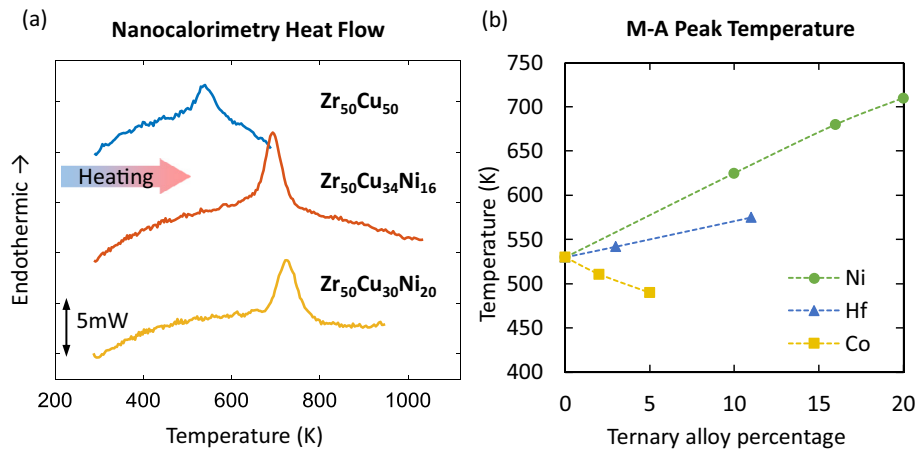


Fig. 4. (a) Comparison of calorimetry results of Cu-Zr-Ni. (b) List of martensite-austenite transformation peak temperatures. The results have an estimated error of ± 5 K.

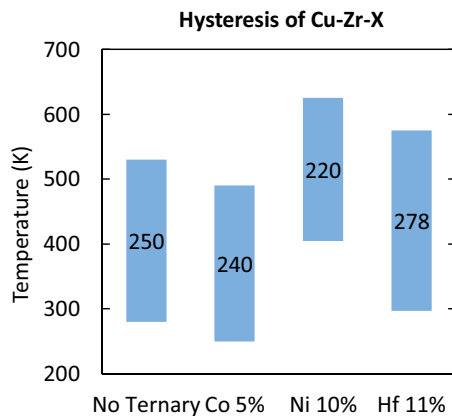


Fig. 5. Hysteresis of martensite-austenite and austenite-martensite transformation peaks. Top of the bar is M-A peak temperature and bottom of the bar is A-M peak temperature. The numbers show hysteresis (± 10 K error).

plates compared with the Ni-containing alloy. The grain size in the samples ranges from 300 nm in the center of the film to 50 nm near the surface. As shown in Fig. 6b, the martensite plates consist of much finer twins. This is in line with the general theory that

martensite grows finely twinned structures to minimize the compatibility strain with the austenite and that result in leaf-like structures with a midrib [44,45]. Multiple diffraction images confirmed the existence of Cm structure. (021) and (001) twin planes were identified. Another monoclinic structure, B19' (P21m space group), has also been reported [20], but was not identified by us. Since Cm is a superstructure of B19' [19], B19' has fewer diffraction spots and its diffraction pattern overlaps with that of Cm. The evidence thus suggests that there were no regions in the sample under investigation that consisted exclusively of B19'.

3.4. Austenite-martensite lattice compatibility

We used *ab initio* simulations to model the B2 and Cm phases of Cu-Zr-X with various concentrations of element X. The lattice parameters of the fully relaxed Cu-Zr-X B2 and Cm structures are listed in Table 1. Table 2 provides a comparison of experimental and computational lattice parameters for martensite. The agreement between experimental and computational values is well within the error of the DFT simulations and the TEM imaging. The lattice parameters of two phases can be used to calculate the transformation matrix, which maps the austenite lattice vectors onto the martensite lattice vectors. James et al. have shown that

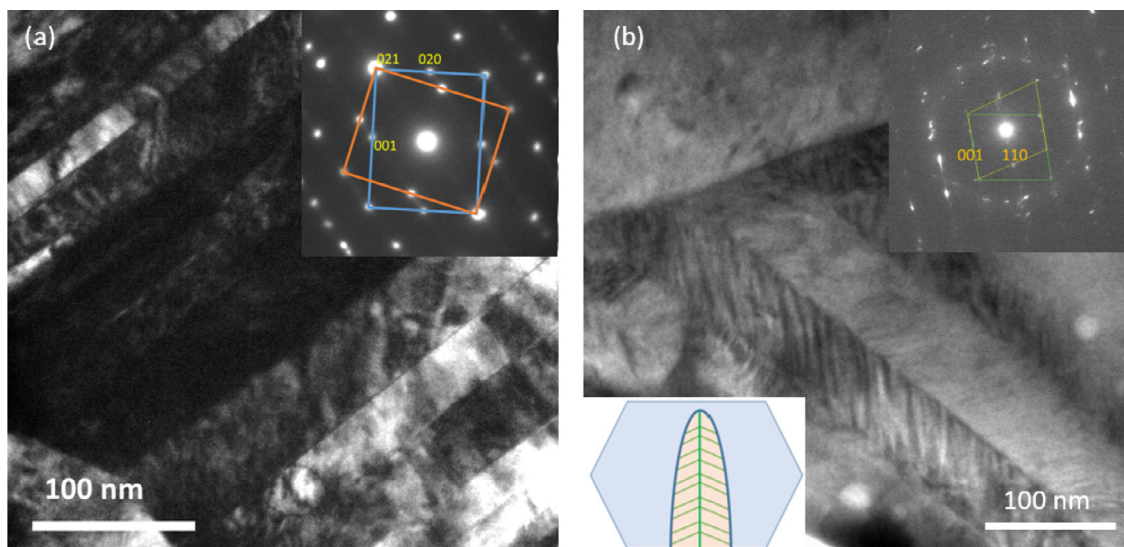


Fig. 6. TEM images and corresponding diffraction patterns of (a) $Zr_{50}Cu_{34}Ni_{16}$ and (b) $Cu_{50}Zr_{39}Hf_{11}$. Inset in (b) shows possible microstructure of martensite growing in austenite.

Table 1
Calculated lattice parameters of Cu-Zr-X. Co and Ni replaces Cu, while Hf replaces Zr in Cu₅₀Zr₅₀.

Unit in Å	Alloying percentage	B2 austenite			Cm martensite			
		a	b	c	a	b	c	gamma
X=Co	1.56	6.58	9.22	4.61	6.59	8.27	5.28	102.80
	3.13	6.61	9.18	4.59	6.59	8.28	5.24	102.45
	6.25	6.63	9.12	4.59	6.60	8.30	5.20	102.17
	12.50	6.51	9.40	4.49	6.66	8.23	5.21	103.63
	18.75	6.46	9.31	4.52	6.64	8.22	5.16	103.07
X=Hf	1.56	6.57	9.23	4.61	6.52	8.30	5.35	103.63
	3.13	6.56	9.23	4.62	6.52	8.30	5.34	103.35
	6.25	6.56	9.18	4.63	6.52	8.31	5.32	103.00
	12.50	6.51	9.25	4.61	6.51	8.29	5.32	103.48
	18.75	6.56	9.19	4.56	6.57	8.21	5.28	103.46
X=Ni	1.56	6.58	9.22	4.61	6.53	8.29	5.35	103.69
	3.13	6.54	9.24	4.62	6.59	8.26	5.27	102.78
	6.25	6.59	9.19	4.60	6.59	8.27	5.24	102.50
	12.50	6.34	9.76	4.46	6.58	8.25	5.24	103.01
	18.75	6.57	9.14	4.57	6.60	8.25	5.18	102.31

Table 2
Comparison of experimental and computational lattice parameters of martensite. The experimental values are from TEM diffraction images (Fig. 6). The computational values are from a linear fit of Table 1.

Unit in Å	Zr ₅₀ Cu ₃₄ Ni ₁₆		Cu ₅₀ Zr ₃₉ Hf ₁₁
	b	c sinβ	c sinβ
Experimental	8.25	5.20	5.23
Computational	8.25	5.11	5.17

the middle eigenvalue (λ_2) of the transformation matrix is a measure for the compatibility between the austenite and the martensite [46,47]. The further the middle eigenvalue diverges from unity, the larger the mismatch on the martensite-austenite habit plane. Following the approach in [48], we computed the transformation matrices and their eigenvalues for the various Cu-Zr-X alloys. The middle eigenvalues are plotted in Fig. 7. It is evident from the figure that Ni and Co bring λ_2 closer to 1, while Hf does not significantly change λ_2 . Based on this result, one would expect the addition of Ni or Co to reduce the strain at the austenite martensite interface and thus reduce the transformation hysteresis as indeed observed experimentally; the addition of Hf, on the other hand,

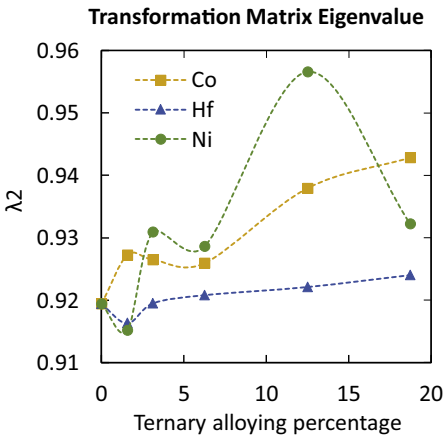


Fig. 7. The second eigenvalue of the austenite-martensite transformation matrix. The second eigenvalue is an indicator of the compatibility between two phases. A unit value signifies no lattice mismatch. The lines connecting the data points are Bezier spline interpolations that serve as guides to the eye. They have no physical meaning.

should leave the hysteresis more or less unchanged, which is not observed. Of course, other factors may also affect hysteresis, e.g., the addition of ternary elements may introduce defects that make the motion of interfaces more difficult.

3.5. Transformation pathway and energy landscape

Thus far, the transformation pathway of B2-Cm has not been studied. Previous work suggests that B2 and Cm structures have crystallographic relationship that resembles NiTi B2-B19' [19]. However, it is not clear why CuZr B2 transforms to Cm, instead of B19'. Using the lattice correspondence, we modelled the B2-Cm energy landscape using four independent parameters. A four-dimensional minimum energy pathway was determined, which was further refined by the solid-state nudged elastic band method (SSNEB). We find that the B2-Cm transformation goes through Cmm2 as an intermediate structure (Fig. 8). The B2-Cmm2 step takes place without an energy barrier, while the Cmm2-Cm step has a small energy barrier that is slightly higher than the energy

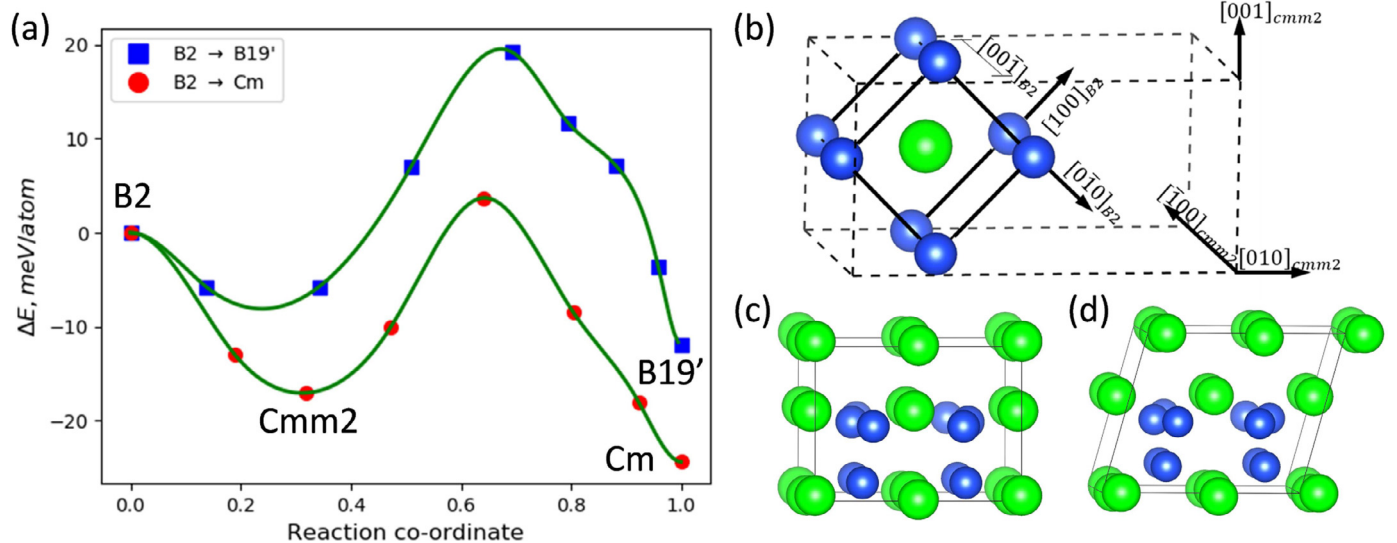


Fig. 8. (a) Transformation pathway from B2 to Cm and B2 to B19'. Cmm2 is proposed as an intermediate structure of B2-Cm. The transformation from B2 to Cmm2 is barrier-less, while the transformation from Cmm2 to Cm has a saddle point that is not much higher in energy than the B2 phase. (b) The lattice correspondence between B2 and Cmm2. (c) and (d) show the structures of Cmm2 and Cm, respectively.

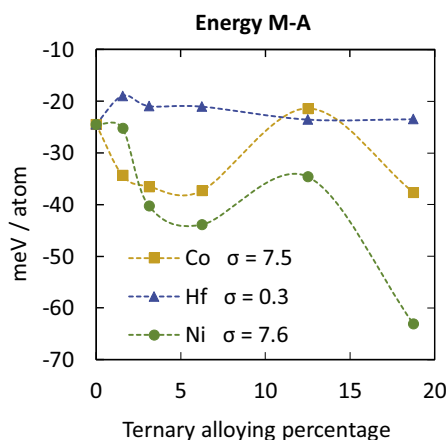


Fig. 9. Energy difference between martensite and austenite. For each composition, several simulations with different atomic site replacements were performed. Each data point represents the minimum-energy configuration for that composition. For a given ternary element, the standard deviation σ (given in meV) is consistent across the composition range for that element. The lines connecting the data points are Bezier spline interpolations that serve as guides to the eye. They have no physical meaning.

of the initial B2 phase. The same figure also shows the transformation of B2 to B19'. The B19' path has a slightly higher energy than the Cm path along the entire length of the transformation path. While the higher energy of the B2-B19' transformation may explain why only the Cm phase is observed in this study, the energy difference between the two paths is quite small and may be overcome at finite temperatures.

The energy differences between the austenite and martensite phases at 0 K obtained from simulations are depicted as a function of composition in Fig. 9. A negative value signifies that the martensite phase is more stable than the austenite. The calculations show that alloying CuZr with either Ni or Co should stabilize the martensite compared to the austenite, suggesting a higher martensitic transformation temperature. Alloying with Hf does not have a significant effect on the energy difference between the two

phases. These conclusions presuppose that there is no third phase that is more stable than either austenite or martensite when the alloying elements are added. In our experiments, Cu-Zr-X samples with 8% Co or more do not form martensite, showing that a negative M-A energy gap does not necessarily imply the formation of martensite.

When comparing the experimental results (Figs. 4 and 5) with the M-A energy gap in Fig. 9, it is clear that the computations and experiments are in agreement for Ni. In Fig. 5, the addition of Hf does not significantly shift the midpoint of transformation temperatures. However, in the case of Co, computations suggest that Co should increase the transformation temperature up to a concentration of 6%, but experiments show the opposite behavior. To rule out finite-temperature effects, calculations for these phases were also performed at finite temperatures (Fig. 10). These simulations took into account quasi-harmonic, electronic, and weak anharmonic contributions. Full anharmonicity was beyond the scope of our efforts, mostly due to the considerable computational expense associated with carrying out full anharmonic phonon calculations over the large, low symmetry unit cells necessary to simulate compositional disorder. With these terms added, we still see the energy difference crosses over zero at higher temperature for both the Ni and Co ternaries.

3.6. Twin boundary energy

It is evident from the results above that the energy difference between pristine martensite and austenite alone cannot explain the observed experimental trends. Energy terms beyond the energies of the pure phases need to be considered. For the martensitic transformation to proceed, martensite crystals need to grow in austenite, creating austenite/martensite interfaces that can have very large compatibility strains depending on the value of λ_2 . These compatibility strains are accommodated by twinning in the martensite and thus have a significant impact on the resulting microstructure. TEM imaging shows that Cu-Zr-X martensite indeed has a finely twinned microstructure (Fig. 6b). This observation leads us to consider the contribution of the twin boundary energy to the total energy of the martensitic phase. The energy

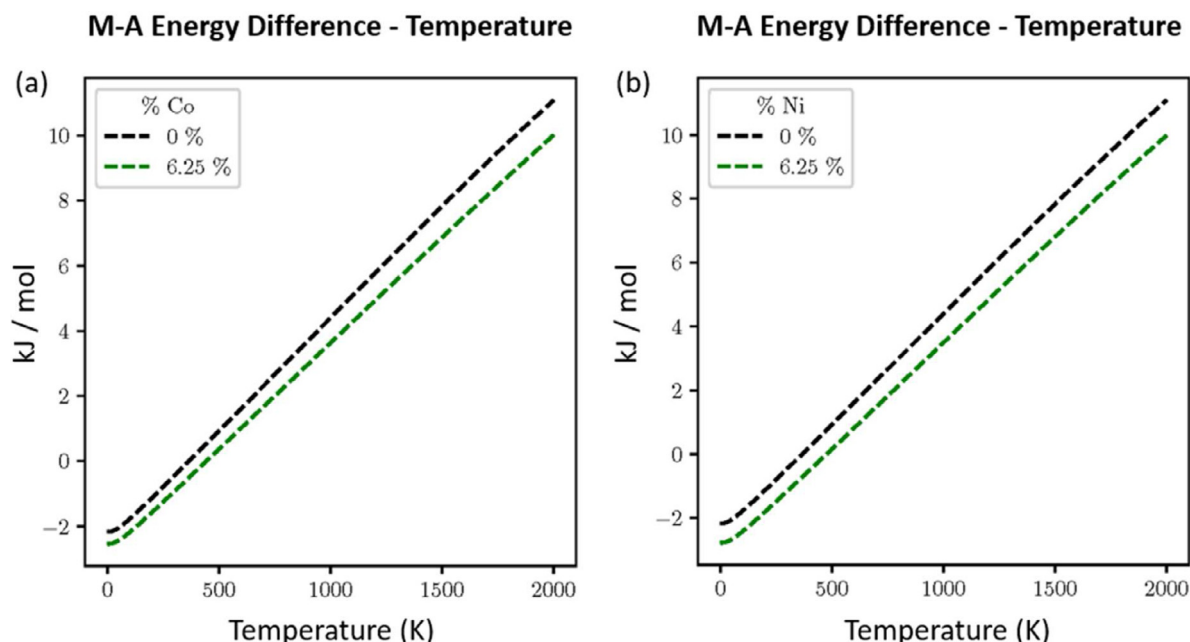


Fig. 10. Finite temperature simulations. Each line shows the energy difference between martensite and austenite of a specific composition. At any given temperature, the M-A energy difference for Ni or Co ternary is larger than pure CuZr.

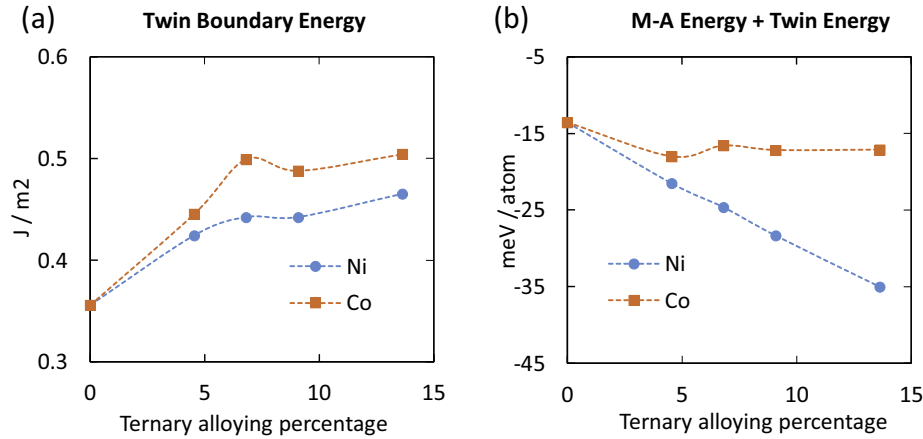


Fig. 11. (a) Twin boundary energy as a function of composition; (b) Total energy difference between the martensite and austenite phases taking into account the presence of the twin boundaries. To reduce errors, the M-A energy is calculated using a linear fit to the energy difference between pristine martensite and austenite in Fig. 9.

of the (021) twin boundary was calculated for the CuZrCo and CuZrNi systems as described earlier. These systems were selected rather than the CuZrHf system because Co and Ni have similar effects on the energy difference between austenite and martensite, but opposite effects in our experiments. The twin boundary energy results are shown in Fig. 11a. It is evident from the figure that both ternary alloys have a higher twin boundary energy than binary CuZr and that the twin boundary energy of CuZrCo is consistently higher than that of CuZrNi. Very recent computational work by Sandoval shows that the twin boundary energy of a (001) twin in NiTi B19' is approximately 0.2 J/m² [49]. Compared to NiTi, the twin boundary energy of Cu-Zr-X is somewhat larger, but of the same order of magnitude.

To evaluate the impact of the twin boundary energy on the energy difference between the martensite and austenite, the twin boundary energy is converted to meV/atom. Because there was no significant variation of the spacing (standard deviation was approximately 1 nm) across different samples or grains as observed by TEM, an average twin spacing of 3.7 nm was used in this calculation. The energy difference between martensite and austenite (Fig. 9) is fitted with a straight line to reduce error, although other forms of interpolation lead to similar conclusions. The results are shown in Fig. 11b. The twin boundary energy has a significant impact on the energy gap between the two phases and this impact is different for different alloying elements: The energy gap increases with Ni content, as before, but remains nearly unchanged with the addition of Co. While there may be some uncertainty in the precise values of the twin boundary energies, it is clear from this example that the martensite twin spacing is small enough for the associated energy terms to alter the energy balance between the two phases. A simple comparison of the energies of the pristine phases is not sufficient to make predictions about the effect of alloying elements on the stability of the martensitic phase.

4. Discussion

4.1. Non-monotonic behavior of *ab initio* simulations

In both Figs. 7 and 9, the value of λ_2 and the energy difference between the martensite and austenite phases are non-monotonic with composition. In Fig. 9, in particular, the data point at 12.5% creates a local maximum in the energy curve for both Co and Ni. The experimental trends in Fig. 4b, on the other hand, shows good linear behavior. To verify that this local maximum is not caused by a poor choice of ternary alloying sites, we have tested various atom replacements (Co/Ni replacing Cu) and reached the lowest-

energy configurations in a 64-atom supercell. Fig. 9 plots all the lowest-energy points among these tests. At 12.5%, the standard deviation is smaller than the fluctuation of the curve itself. Therefore, in the scope of *ab initio* simulations, the non-monotonic behavior seems to have an electronic origin that remains to be elucidated. It should be noted that the compositions where the energy has a local maximum, result in structures with relatively larger monoclinic angles as compared to other compositions (Table 1). We note that in Huang's work on NiTi shape memory alloys [50], the experimentally measured monoclinic angle of the B19' phase is always smaller than the computed angle. Huang et al. attributed this discrepancy to the stress-free condition of *ab initio* simulations. In a later study, Haskins showed that the monoclinic angle of B19' is sensitive to entropic effects [51]. Up to date, there is no definitive answer to this discrepancy in the NiTi system. In this work, the computed angles of the Cm phase are close to the experimental value of the binary CuZr alloy (105°) [19,20] with only small fluctuations. We expect that these angles are similarly sensitive to entropic effects and the fluctuations may not be actually observed at finite temperatures. As a result, we also expect that the corresponding small energy differences may not be observed. Following this line of reasoning, a linear fit to the energy data was used capture the trend in the data and to compute the energy of the twinned martensite.

4.2. Balance of twin boundary energy and M-A strain energy

The existence of twin boundaries in martensite adds to the total energy of the martensitic phase, making it less favorable relative to the parent austenitic phase. The twin boundaries are necessary to accommodate the compatibility strains associated with martensitic transformations. In Fig. 11b, the contribution of the twin boundary energy to the total energy was calculated using the experimentally measured twin spacing. This twin spacing arises from a balance between the total twin boundary energy and transformation strain energy. Here, we use a simple energy argument to derive an estimate of the twin spacing and the magnitude of the strain energy from *ab initio* parameters. Suppose that martensitic growth occurs as shown schematically in Fig. 12. Because twinning localizes the compatibility strain field to the M-A interface, we assume the strain energy is uniformly distributed in the cylindrical volumes marked by the red circles in Fig. 12. For a single twin plate, we take the strain energy per unit depth equal to

$$E_{\text{Strain}} = 2 * \frac{1}{2} Y (1 - \lambda_2)^2 * \frac{\pi t^2}{4}, \quad (3)$$

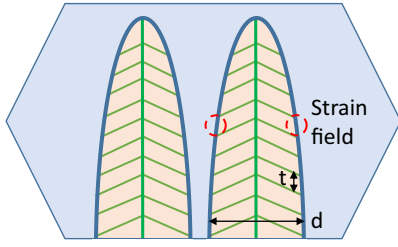


Fig. 12. Schematic of martensite growth mode. The yellow regions are large martensite plates. The blue region is austenite; the green lines are twin planes. The red circles represent the cylindrical volumes that is affected by the M-A interfacial strain in individual small twin plates. (For interpretation of the references to colour in this figure legend, the reader is referred to the web version of this article.)

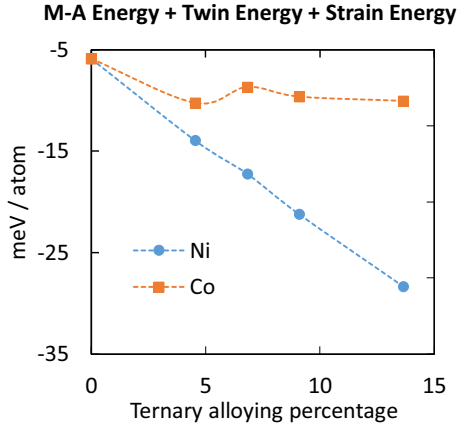


Fig. 13. Adding M-A energy gap, twin boundary energy, and strain energy. Both Ni and Co-alloys shift towards the positive side.

where Y is the elastic modulus of CuZr (75 GPa [52]), t is the twin width, and λ_2 is the second eigenvalue of the transformation matrix. Eq. (3) assumes linear elasticity and ignores any stress relaxation as a result of defect formation. The twin boundary energy for a single twin plate is then approximately

$$E_{TB} = \gamma d, \quad (4)$$

where γ is the twin boundary energy per unit area, and d is the width of the martensite plates. The total energy per unit volume of martensite is then given by

$$E_{Total} = \frac{1}{td} (E_{Strain} + E_{TB}) = \frac{\pi t}{4d} Y (1 - \lambda_2)^2 + \frac{\gamma}{t}. \quad (5)$$

The energy associated with the compatibility strain and twin boundaries is minimized when the twin spacing is given by

$$t = \frac{2}{1 - \lambda_2} \sqrt{\frac{\gamma d}{\pi Y}}. \quad (7)$$

Taking $\lambda_2 = 0.93$ (Fig. 7), $\gamma = 0.5$ J/m² (Fig. 11a), and $d = 30$ nm (Fig. 6), yields a twin spacing of approximately 7.2 nm. This is on the same order of magnitude of the actual twin spacing (3.7 nm), albeit somewhat larger. We attribute this to the fact that Eq. (3) does not account for the entire compatibility strain field. If the actual strain energy is larger, a finer twin structure is needed to reduce it. Fig. 13 shows the energy difference between martensite and austenite, taking into account both the compatibility strain energy and twin boundary energy as calculated from the *ab initio* simulations. It is clear that these extra energy terms have a significant impact on both the magnitude of the energy difference and its dependence on composition. Based on these results, we suggest that *ab initio* simulations are a useful tool in guiding the experimental development of shape memory alloys, provided the energy

terms associated with the fine twin structure are taken into account.

5. Conclusions

We have carried out a detailed investigation of the Cu-Zr-X (X=Ni/Co/Hf) shape memory alloy system using both experimental and computational methods. We used nanocalorimetry to measure the phase transformations behavior, and *ab initio* simulations to evaluate the lattice parameters, relative phase stability, the transformation pathway, and twin boundary energy as a function of composition. Our experiments show that the kinetics of the eutectoid reaction that produces the austenitic phase is faster in the Ni-containing alloy than in both the CuZr and the Co- or Hf-containing alloys. Alloying CuZr with either Ni or Co reduces the hysteresis of the martensitic transformation, while Hf increases hysteresis. These observations are in agreement with the trend of the middle eigenvalue of the martensitic transformation matrix, which is calculated from the *ab initio* lattice parameters. Simulations show that the energy difference between pristine martensite and austenite decreases with the addition of either Ni or Co, and remains more or less unchanged with the addition of Hf. These observations suggest that both Ni and Co should increase the transformation temperature of CuZr, while Hf has little effect. Experimentally, it is observed that adding Co reduces the martensitic transformation temperature. We attribute this to the fact that martensite does not grow in austenite as a pristine phase, but is heavily twinned as a result of the compatibility strains at the martensite/austenite interface. Adding the energy terms representing the twin boundaries and the compatibility strain has a significant impact on both the magnitude of the energy difference between the two phases and its dependence on composition, bringing experiment and computation to a closer agreement. Based on these results, we suggest that *ab initio* simulations are a useful tool in guiding the experimental development of shape memory alloys, provided the appropriate energy terms are taken into account. Additionally, experimental observations have led to further investigation of the relevant energetics associated with the martensitic transformations.

Declaration of Competing Interest

The authors declare that they have no known competing financial interests or personal relationships that could have appeared to influence the work reported in this paper.

Acknowledgments

This work was supported by the Air Force Office of Scientific Research under Grant No. FA9550-16-1-0180 (Program Manager: Ali Sayir). It was performed in part at the Center for Nanoscale Systems at Harvard University, which is supported by the National Science Foundation under award No. ECCS-1541959, and at the Materials Research Science and Engineering Center at Harvard University, which is supported by the National Science Foundation under Award No. DMR-1420570. YM acknowledges support from the National Science Foundation under Award No. DMR-1808162. *Ab Initio* calculations were carried out at the Texas A&M High Performance Research Computing Facility, using the Terra and Ada Clusters.

References

- [1] J. Ma, I. Karaman, R.D. Noebe, High temperature shape memory alloys, Int. Mater. Rev. 55 (2010) 257–315, doi:10.1179/095066010X12646898728363.

- [2] J. DeCastro, K. Melcher, R. Noebe, System-Level design of a shapememory-actuator for activeclearancecontrol in the high-pressure turbine, in: Proceedings of the 47th AIAA/ASME/SAE/ASEE Joint Propulsion Conference & Exhibit, American Institute of Aeronautics and Astronautics, Reston, Virginia, 2012, doi:10.2514/6.2005-3988.
- [3] G.S. Firstov, J. Van Humbeeck, Y.N. Koval, High temperature shape memory alloys problems and prospects, J. Intell. Mater. Syst. Struct. 17 (2006) 1041–1047, doi:10.1177/1045389X06063922.
- [4] P.K. Kumar, U. Desai, J.A. Monroe, D.C. Lagoudas, I. Karaman, G. Bigelow, R.D. Noebe, Experimental investigation of simultaneous creep, plasticity and transformation of Ti50.5Pd30Ni19.5 high temperature shape memory alloy during cyclic actuation, Mater. Sci. Eng. A. 530 (2011) 117–127, doi:10.1016/j.msea.2011.09.051.
- [5] E. Bonnot, R. Romero, L. Mañosa, E. Vives, A. Planes, Elastocaloric effect associated with the martensitic transition in shape-memory alloys, Phys. Rev. Lett. 100 (2008) 125901, doi:10.1103/PhysRevLett.100.125901.
- [6] W.L. Benard, H. Kahn, A.H. Heuer, M.A. Huff, Thin-film shape-memory alloy actuated micropumps, J. Microelectro. Mech. Syst. 7 (1998) 245–251, doi:10.1109/84.679390.
- [7] D. Xue, D. Xue, R. Yuan, Y. Zhou, P.V. Balachandran, X. Ding, J. Sun, T. Lookman, An informatics approach to transformation temperatures of NiTi-based shape memory alloys, Acta Mater 125 (2017) 532–541, doi:10.1016/j.actamat.2016.12.009.
- [8] W. Gao, X. Meng, G. Song, W. Cai, L. Zhao, Empirical mapping of ZrCu-based alloys with valence electrons versus transformation temperatures, Sci. China Mater. 59 (2016) 151–157, doi:10.1007/s40843-016-0124-z.
- [9] Y. Motemani, P.J. McCluskey, C. Zhao, M.J. Tan, J.J. Vlassak, Analysis of Ti-Ni-Hf shape memory alloys by combinatorial nanocalorimetry, Acta Mater 59 (2011) 7602–7614, doi:10.1016/j.actamat.2011.08.026.
- [10] P.J. McCluskey, C. Zhao, O. Kfir, J.J. Vlassak, Precipitation and thermal fatigue in Ni-Ti-Zr shape memory alloy thin films by combinatorial nanocalorimetry, Acta Mater 59 (2011) 5116–5124, doi:10.1016/j.actamat.2011.04.043.
- [11] P.J. McCluskey, J.J. Vlassak, Combinatorial nanocalorimetry, J. Mater. Res. 25 (2010) 2086–2100, doi:10.1557/jmr.2010.0286.
- [12] J. Zheng, Y. Miao, H. Zhang, S. Chen, D. Lee, R. Arróyave, J.J. Vlassak, Phase transformations in equiatomic CuZr shape memory thin films analyzed by differential nanocalorimetry, Acta Mater 159 (2018) 320–331, doi:10.1016/j.actamat.2018.08.015.
- [13] G. Kresse, J. Furthmüller, Software VASP, vienna (1999), Phys. Rev. B. 54 (1996) 169.
- [14] J.P. Perdew, K. Burke, Y. Wang, Generalized gradient approximation for the exchange-correlation hole of a many-electron system, Phys. Rev. B. 54 (1996) 16533–16539, doi:10.1103/PhysRevB.54.16533.
- [15] J.P. Perdew, Y. Wang, Accurate and simple analytic representation of the electron-gas correlation energy, Phys. Rev. B. 45 (1992) 13244–13249, doi:10.1103/PhysRevB.45.13244.
- [16] P.E. Blöchl, Projector augmented-wave method, Phys. Rev. B. 50 (1994) 17953–17979, doi:10.1103/PhysRevB.50.17953.
- [17] M. Methfessel, A.T. Paxton, High-precision sampling for Brillouin-zone integration in metals, Phys. Rev. B. 40 (1989) 3616–3621, doi:10.1103/PhysRevB.40.3616.
- [18] P.E. Blöchl, O. Jepsen, O.K. Andersen, Improved tetrahedron method for Brillouin-zone integrations, Phys. Rev. B. 49 (1994) 16223–16233, doi:10.1103/PhysRevB.49.16223.
- [19] D. Schryvers, G.S. Firstov, J.W. Seo, J. Van Humbeeck, Y.N. Koval, Unit cell determination in CuZr martensite by electron microscopy and X-ray diffraction, Scr. Mater. 36 (1997) 1119–1125, doi:10.1016/S1359-6462(97)00003-1.
- [20] J.W. Seo, D. Schryvers, TEM investigation of the microstructure and defects of CuZr martensite. part I: morphology and twin systems, Acta Mater 46 (1998) 1165–1175, doi:10.1016/S1359-6454(97)00333-9.
- [21] A. Talapatra, An ab initio investigation of thermoelastic phase transformations in transition metal alloys, (2015). <https://oaktrust.library.tamu.edu/handle/1969.1/156447>, (accessed June 3, 2019).
- [22] M.D. McKay, R.J. Beckman, W.J. Conover, Comparison of three methods for selecting values of input variables in the analysis of output from a computer code, Technometrics 21 (1979) 239–245, doi:10.1080/00401706.1979.10489755.
- [23] I. Marcos-Alcalde, J. Setoain, J.L. Mendieta-Moreno, J. Mendieta, P. Gómez-Puertas, MEPSA: minimum energy pathway analysis for energy landscapes: fig. 1, Bioinformatics 31 (2015) btv453, doi:10.1093/bioinformatics/btv453.
- [24] D. Sheppard, P. Xiao, W. Chemelewski, D.D. Johnson, G. Henkelman, A generalized solid-state nudged elastic band method, J. Chem. Phys. 136 (2012) 074103, doi:10.1063/1.3684549.
- [25] S. Ivantchev, E. Kroumova, G. Madariaga, J.M. Pérez-Mato, M.I. Aroyo, SUBGROUPGRAPH: a computer program for analysis of group-subgroup relations between space groups, J. Appl. Crystallogr. (2000), doi:10.1107/S0021889800007135.
- [26] A. Zunger, S.-H. Wei, L.G. Ferreira, J.E. Bernard, Special quasirandom structures, Phys. Rev. Lett. 65 (1990) 353–356, doi:10.1103/PhysRevLett.65.353.
- [27] S. Wei, M.Y. Chou, *Ab initio* calculation of force constants and full phonon dispersions, Phys. Rev. Lett. 69 (1992) 2799–2802, doi:10.1103/PhysRevLett.69.2799.
- [28] A. van de Walle, M. Asta, G. Ceder, The alloy theoretic automated toolkit: a user guide, Calphad 26 (2002) 539–553, doi:10.1016/S0364-5916(02)80006-2.
- [29] A. van de Walle, G. Ceder, The effect of lattice vibrations on substitutional alloy thermodynamics, Rev. Mod. Phys. 74 (2002) 11–45, doi:10.1103/RevModPhys.74.11.
- [30] T. Duong, S. Gibbons, R. Kinra, R. Arróyave, *Ab-initio* approach to the electronic, structural, elastic, and finite-temperature thermodynamic properties of Ti₂X (X = Al or Ga and x = c or N), J. Appl. Phys. 110 (2011) 093504, doi:10.1063/1.3652768.
- [31] Z. Altounian, T. Guo-hua, J.O. Strom-Olsen, Crystallization characteristics of Cu-Zr metallic glasses from Cu 70 Zr 30 to Cu 25 Zr 75, J. Appl. Phys. 53 (2003) 4755–4760, doi:10.1063/1.331304.
- [32] D. Lee, B. Zhao, E. Perim, H. Zhang, P. Gong, Y. Gao, Y. Liu, C. Toher, S. Curtarolo, J. Schroers, J.J. Vlassak, Crystallization behavior upon heating and cooling in Cu₅₀Zr₅₀ metallic glass thin films, Acta Mater 121 (2016) 68–77, doi:10.1016/j.actamat.2016.08.076.
- [33] X.J. Liu, H.H. Zhang, C.P. Wang, K. Ishida, Experimental determination and thermodynamic assessment of the phase diagram in the Co-Zr system, J. Alloys Compd. 482 (2009) 99–105, doi:10.1016/j.jallcom.2009.04.032.
- [34] P. Nash, C.S. Jayanthi, The Ni–Zr (Nickel–Zirconium) system, Bull. Alloy Phase Diagrams. 5 (1984) 144–148, doi:10.1007/BF02868950.
- [35] P.R. Subramanian, D.E. Laughlin, The Cu–Hf (copper–hafnium) system, Bull. Alloy Phase Diagrams. 9 (1988) 51–56, doi:10.1007/BF02877460.
- [36] E. Perim, D. Lee, Y. Liu, C. Toher, P. Gong, Y. Li, W.N. Simmons, O. Levy, J.J. Vlassak, J. Schroers, S. Curtarolo, Spectral descriptors for bulk metallic glasses based on the thermodynamics of competing crystalline phases, Nat. Commun. 7 (2016) 12315, doi:10.1038/ncomms12315.
- [37] T. Kosorukova, G. Firstov, Y. Koval, P. Verhovlyuk, J. Van Humbeeck, H. Noel, Structural phase transformations and shape memory effect in ZrCu along with Ni and Hf additions, in: Proceedings of the MATEC Web of Conferences, 33, 2015, p. 06005, doi:10.1051/mateconf/20153306005.
- [38] C.A. Biffi, A. Figini, A. Tuissi, Influence of compositional ratio on microstructure and martensitic transformation of CuZr shape memory alloys, Intermetallics 46 (2014) 4–11, doi:10.1016/j.intermet.2013.10.018.
- [39] F. Meng, K. Tsuchiya, S. Li, Y. Yokoyama, Influence of Ni on stability of martensitic transformation in Zr₅₀Cu₅₀-xNi, J. Alloys Compd 577 (2013) 136–140, doi:10.1016/j.jallcom.2012.01.089.
- [40] C.A. Biffi, A. Figini, A. Tuissi, CuZr based shape memory alloys: effect of Cr and Co on the martensitic transformation, Mater. Sci. Forum (2013) 167–171, doi:10.4028/www.scientific.net/MSF.738-739.167.
- [41] F.A. Javid, N. Mattern, S. Pauly, J. Eckert, Martensitic transformation and thermal cycling effect in Cu–Co–Zr alloys, J. Alloys Compd 509 (2011) S334–S337, doi:10.1016/j.jallcom.2011.01.186.
- [42] G.S. Firstov, J. Van Humbeeck, Y.N. Koval, Peculiarities of the martensitic transformation in ZrCu intermetallic compound - potential high temperature sma, Le J. Phys. IV. 11 (2001) Pr8-481-Pr8-486, doi:10.1051/jp4:2001880.
- [43] W.-S. Ko, S.B. Maisel, B. Grabowski, J.B. Jeon, J. Neugebauer, Atomic scale processes of phase transformations in nanocrystalline NiTi shape-memory alloys, Acta Mater 123 (2017) 90–101, doi:10.1016/j.actamat.2016.10.019.
- [44] R.P. Reed, The plate-like martensite transformation in Fe–Ni alloys, Acta Metall (1967), doi:10.1016/0001-6160(67)90004-1.
- [45] T. Waiz, The self-accommodated morphology of martensite in nanocrystalline NiTi shape memory alloys, Acta Mater (2005), doi:10.1016/j.actamat.2005.01.033.
- [46] Y. Song, X. Chen, V. Dabade, T.W. Shield, R.D. James, Enhanced reversibility and unusual microstructure of a phase-transforming material, Nature 502 (2013) 85–88, doi:10.1038/nature12532.
- [47] R.D. James, Z. Zhang, R.D. James, Z. Zhang, in: A Way to Search for Multiferroic Materials With “Unlikely” Combinations of Physical Properties, Springer, Berlin, Heidelberg, 2005, pp. 159–175, doi:10.1007/3-540-31631-0_9.
- [48] R.D. James, K.F. Hane, Martensitic transformations and shape-memory materials, Acta Mater 48 (2000) 197–222, doi:10.1016/S1359-6454(99)00295-5.
- [49] L. Sandoval, J.B. Haskins, J.W. Lawson, Stability, structure, and suppression of the martensitic transition temperature by B19' compound twins in NiTi: ab initio and classical simulations, Acta Mater 154 (2018) 182–189, doi:10.1016/j.actamat.2018.05.016.
- [50] X. Huang, G.J. Ackland, K.M. Rabe, Crystal structures and shape-memory behaviour of NiTi, Nat. Mater. 2 (2003) 307–311, doi:10.1038/nmat884.
- [51] J.B. Haskins, A.E. Thompson, J.W. Lawson, Ab initio simulations of phase stability and martensitic transitions in NiTi, Phys. Rev. B. 94 (2016) 1–10, doi:10.1103/PhysRevB.94.214110.
- [52] J. Du, B. Wen, R. Melnik, Y. Kawazoe, Phase stability, elastic and electronic properties of Cu–Zr binary system intermetallic compounds: a first-principles study, J. Alloys Compd 588 (2014) 96–102, doi:10.1016/j.jallcom.2013.11.018.